BIOFILMS

Cell position fates and collective fountain flow in bacterial biofilms revealed by light-sheet microscopy

Boyang Qin[1,2], Chenyi Fei[1,3], Andrew A. Bridges[1,4], Ameya A. Mashruwala[1,4], Howard A. Stone[2], Ned S. Wingreen[1,3,5], Bonnie L. Bassler[1,4]*

Bacterial biofilms represent a basic form of multicellular organization that confers survival advantages to constituent cells. The sequential stages of cell ordering during biofilm development have been studied in the pathogen and model biofilm-former *Vibrio cholerae*. It is unknown how spatial trajectories of individual cells and the collective motions of many cells drive biofilm expansion. We developed dual-view light-sheet microscopy to investigate the dynamics of biofilm development from a founder cell to a mature three-dimensional community. Tracking of individual cells revealed two distinct fates: one set of biofilm cells expanded ballistically outward, while the other became trapped at the substrate. A collective fountain-like flow transported cells to the biofilm front, bypassing members trapped at the substrate and facilitating lateral biofilm expansion. This collective flow pattern was quantitatively captured by a continuum model of biofilm growth against substrate friction. Coordinated cell movement required the matrix protein RbmA, without which cells expanded erratically. Thus, tracking cell lineages and trajectories in space and time revealed how multicellular structures form from a single founder cell.

Complex organizations of cells can emerge from simple starting points (*1–3*). For example, both eukaryotic embryos and prokaryotic biofilms arise from single founder cells (*4–7*). In both cases, development via cell division produces three-dimensional (3D) collections of cells encased in extracellular matrices. Despite a common origin, descendant cells in both systems differ in spatial positions, nutrient access, signaling gradients, and states of mechanical stress (*8–14*). Lineage and cell trajectory maps have been made for cells in developing embryos (*4, 5, 15*), yet no such maps exist for bacterial biofilms. Many fundamental activities that transcend all of biology are relevant in bacterial biofilms. Cells in biofilms communicate, undertake both individual and collective tasks, enjoy survival benefits conferred by the multicellular structure and internal organization, and display clear differences in temporal and spatial gene expression patterns (*11, 12, 16–18*). Thus, tracing lineages and spatial trajectories of bacterial cells in biofilms is essential to understanding biofilm development and to identifying the underlying biological and physical principles governing multicellular development. A roadblock in this undertaking is that conventional confocal microscopy is insufficient to achieve the spatial and temporal resolution required to map cell paths in densely packed biofilms containing micrometer-sized bacteria (*19*).

In this study, we combined dual-view light-sheet microscopy (*5, 20–23*) with intracellular puncta labeling technology (*24, 25*) to explore individual and collective cell dynamics and developmental patterns in living wild-type (WT) *Vibrio cholerae* biofilms (Fig. 1, A and B, and movies S1 and S2). We found that biofilm cells had one of two cell fates: They either became trapped by the substrate to anchor the biofilm, or they moved ballistically to expand the biofilm. We observed an emergent collective fountain-like cell flow that coordinated global biofilm expansion driving its overall morphology. RbmA, an extracellular matrix protein secreted by biofilm cells, was required for coherent cell motion.

Dual-view light-sheet microscopy enables mapping of individual cell trajectories

To overcome limitations in temporal resolution of conventional confocal microscopy, we adapted a dual-view inverted selective plane illumination microscope (diSPIM) for the study of prokaryotic cells in biofilms (*20, 21*). We achieved isotropic resolution in the axial and lateral directions (Fig. 1C and fig. S1) with photobleaching an order of magnitude lower (Fig. 1D and fig. S2) than in traditional spinning disk confocal microscopy at equivalent magnification. We used diSPIM to image isolated biofilm clusters for 16 hours at a time resolution of 3 min, which allowed us to follow individual cells in time. To spatially resolve densely packed micrometer-sized bacteria and overcome the optical sectioning limitations of light-sheet microscopy, we introduced constitutively produced mNeonGreen-μNS (mNG-μNS) fluorescent protein (tables S1 and S2) that forms a defined cytoplasmic punctum in each cell (*25*). The avian reovirus protein μNS self-assembles to form a single particle in the bacterial cytoplasm. Once

formed, a punctum exhibited minimal intracellular displacement (fig. S3). During successive divisions, the punctum was inherited by the mother cell, and the daughter cell gradually gained a new punctum (Fig. 1E and fig. S4). Because each punctum persisted along only one branch of the lineage (Fig. 1F), the punctum trace provided a high-resolution representation of a cell's trajectory over a prolonged period. This strategy enabled sufficient spatiotemporal resolution to map individual cell trajectories and cell positions for up to 10^4 cells over the full course of biofilm development (movies S3 and S4).

The Brownian-to-ballistic transition in cell motion underlies the 2D to 3D biofilm architectural transition

Time-resolved cell trajectories showed a distinct transition in cell motion during biofilm development. In the initial phase (Fig. 1, G and H, 0 to 5 hours), in which the biofilm grew predominantly in the lateral plane, cells frequently changed their directions of motion, akin to random walks. As the biofilm developed (Fig. 1, G and H, 5 to 10 hours), however, individual cells began to engage in persistent and straight trajectories, which dominate the bulk of the biofilm at the later stage (Fig. 1, G and H, 10 to 15 hours). Biofilm expansion is driven by cell division, extracellular matrix secretion, and osmotic swelling (*26*). This kinematic transition in cell movement was quantified by measuring the mean squared displacement (MSD) of cell trajectories versus lag time τ, the time offset between cell location observations (Fig. 2, A and B), where the scaling exponent ν (MSD ~ $τ^ν$) characterizes cell motions. The MSD exponent ν is independent of cell movement speeds and biofilm expansion rates but dependent on how strongly cell trajectories are correlated in time. At early times (1 to 6 hours), ν was around 1.2, suggesting that cell motion is close to random and Brownian (Fig. 2C and fig. S5). At around 7 hours, ν rapidly increased to a plateau value of 1.8, indicating a transition to nearly straight and persistent cell trajectories. The Brownian-to-ballistic transition of cell motion coincided with the transition from predominantly lateral biofilm expansion to accelerated vertical expansion (Fig. 2D), that is, a transition from two to three dimensions.

Ballistic motion is driven by matrix production, and loss of matrix alters cell motion

The dynamical and architectural transitions of cells in *V. cholerae* biofilms require the extracellular *Vibrio* polysaccharide (Vps) (*27, 28*). A ΔvpsL mutant that does not produce Vps adhered to the substrate, but after division, most daughter cells were released. Presumably, in the absence of polysaccharide matrix, Vps-associated matrix proteins that promote cell-cell adhesion are not retained (*29–31*). The

[1]Department of Molecular Biology, Princeton University, Princeton, NJ 08544, USA. [2]Department of Mechanical and Aerospace Engineering, Princeton University, Princeton, NJ 08544, USA. [3]Lewis-Sigler Institute for Integrative Genomics, Princeton University, Princeton, NJ 08544, USA. [4]The Howard Hughes Medical Institute, Chevy Chase, MD 20815, USA. [5]Princeton Center for Theoretical Science, Princeton University, Princeton, NJ 08544, USA.
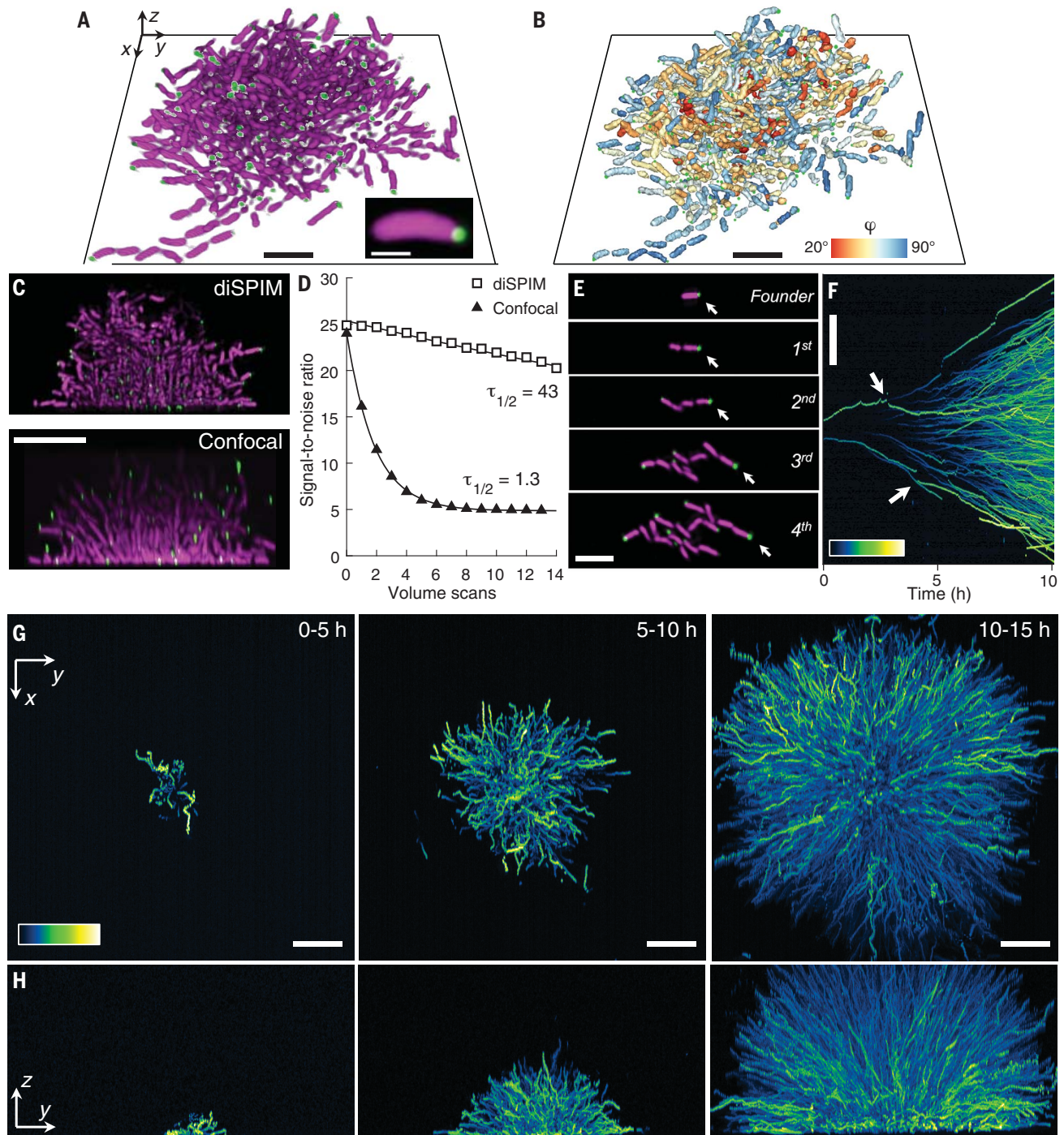*Corresponding author. Email: bbassler@princeton.edu

Fig. 1. Single-cell tracking of WT *V. cholerae* biofilm cells using dual-view light-sheet microscopy and a cytoplasmic fluorescent protein marker. (**A**) 3D view of biofilm cells that constitutively produced mScarlet-I (cell contour) and an mNeonGreen-μNS protein fusion (puncta). Scale bar, 10 μm. (Inset) mNeonGreen-μNS localization at the cell pole. Scale bar, 1 μm. (**B**) Segmented cells and mNeonGreen-μNS puncta (green dots). Colors denote cell orientation φ (angle between cell long axis and the +z axis). (**C**) Side view of a biofilm cluster imaged using light-sheet microscopy (diSPIM) versus spinning disk confocal microscopy. Scale bar, 10 μm. (**D**) Comparison of photobleaching by diSPIM and confocal microscopy measured as the fluorescence signal-to-noise ratio (SNR) of biofilm clusters undergoing repeated volume scans of identical initial SNR in

the shot-noise dominated regime (table S3). Curves represent exponential fits; $\tau_{1/2}$ denotes number of volume scans to reduce SNR by half. (**E**) Four successive cell divisions showing inheritance of the mNeonGreen-μNS puncta. Arrows indicate the punctum in the founder cell. Scale bar, 10 μm. (**F**) Space-time kymograph of mNeonGreen-μNS puncta (in the lateral coordinate y over biofilm development time) shows cell divisions (arrows) and cell lineage traces. Scale bar, 5 μm. Color bar indicates mNeonGreen intensity (arbitrary units, a.u.). (**G**) Top-view projections of biofilm cell trajectories at 3-min time resolution obtained from particle tracking. Color bar indicates mNeonGreen intensity (a.u.). Scale bars, 10 μm. (**H**) Side-view projections of the tracked cell trajectories in (G), with identical scale and color code.

biofilm, as a result, did not transition from the 2D to the 3D morphology. The MSD exponents at the beginning of the experiments (<3 hours) were comparable among the mutants, which all underwent surface attachment and had similar division rates. We observed that substrate-bound $\Delta vpsL$ cells exhibited suppressed cell movement; the cell MSD decreased over time (Fig. 2B) and reached a scaling exponent of $\nu \approx 0.5$ at 16 hours (Fig. 2, B and C), implying subdiffusive cell motion and increased trapping at the surface over time. By contrast, the rugose (Rg) strain with a mutation that drives over-production of extracellular matrix (32) progressed to ballistic-type motion and achieved a plateau MSD exponent similar to that of WT (Fig. 2C and fig. S5).

Cell trapping occurs near the substrate and early in biofilm development

Is cell trapping a consequence of proximity to the substrate for WT cells? To quantify trapping, we defined a dimensionless trapping parameter α as the fraction of a cell's displacements that does not contribute to the net (end-to-end) displacement of that cell's trajectory (33). Here, $\alpha = 0$ implies a persistent motion in one direction (transport), while $\alpha = 1$ implies a trajectory that meanders and eventually returns to its starting point (trapping). For WT biofilm cells, high levels of trapping α occurred in the biofilm core (planar radius $\rho \leq 18\ \mu m$ and height $z \leq 4\ \mu m$), where cells essentially remained fixed in space (Fig. 3A). These cells were trapped at the substrate, moving only minimally over the course of biofilm development (Fig. 3A). Compared to the entire population of biofilm cells, which was dominated by cells moving with straight trajectories ($\alpha \approx 0$),

the group of cells that localized near the substrate ($z \leq 4\ \mu m$) at any time experienced much stronger trapping (Fig. 3B). Because the biofilm morphology was initially predominantly two-dimensional, cells born early (0 to 7 hours) were more likely to remain trapped near the substrate than cells born later (12 to 16 hours) (Fig. 3C).

Biofilm expansion is inhibited near the substrate

Given that cells near the substrate experienced trapping, we were curious whether biofilm expansion was also hindered near the substrate, that is, in the lateral plane. To probe this possibility, we divided WT cell trajectories into four position-dependent subgroups according to their trajectory polar angle ϕ relative to the z axis in the spherical coordinate system (Fig. 3D and fig. S6) and compared their average radial expansion speeds u_r (Fig. 3, E and F). For cells distant from the substrate ($0° \leq \phi \leq 68°$) (Fig. 3E), expansion speed was roughly linear with radial distance r, which implied exponential growth in biofilm volume and cell growth and division rates that were uniform along the biofilm radius. By contrast, cells near the substrate ($68° \leq \phi \leq 90°$) (Fig. 3, E and F) had markedly lower u_r, which deviated from a linear profile. The reduced u_r of cells at the substrate were maintained throughout the three indicated biofilm development time periods (Fig. 3F) and at different radial positions (fig. S7C).

Continuum modeling reveals that substrate friction reduces biofilm expansion near the substrate

We hypothesized that the reduced expansion speed of cells near the substrate is due to friction at the biofilm-substrate interface. To

test this hypothesis, we developed continuum models that consider uniform and isotropic biofilm growth in the presence of substrate friction. Biofilms are viscoelastic materials (34–36). In this study, we considered two extremes: treating the *V. cholerae* biofilm as a viscous fluid or as a hyperelastic solid. We found that the two models yield similar overall shape development (fig. S8), but the fluid model, which we focus on here, better describes the large deformations and time evolution that occur in a growing biofilm. The friction with the substrate, which presumably arises from binding and unbinding of biofilm extracellular polymers and proteins (37), is modeled as viscous drag (33). The expansion velocity field of the modeled biofilm is obtained by solving the internal force balance (33). Indeed, in close agreement with the experimental biofilms, the modeling results show reduced cell motion near the substrate compared to that in the bulk (Fig. 3, G and H).

### An emergent fountain-like flow drives 3D biofilm expansion

How do the dynamical motions of *V. cholerae* biofilm cells drive overall biofilm expansion? To monitor the fates of individual cells, we defined three types of cell motion based on the deviation in cell trajectories from strictly radial motion. This deviation was measured by the end-to-end change in polar angle $\Delta\phi$ for each cell trajectory (Fig. 4A and movie S5). While 60% of the biofilm cells expanded radially with very small angular deviations ($|\Delta\phi| < 5°$), two subsets of cells that originated near the biofilm core demonstrated substantial deviation from radial expansion: one group moved vertically away from the substrate (Fig. 4A, red), while the other group moved upward initially and then curved back down (Fig. 4A, blue), leapfrogging cells that were trapped at the substrate (Fig. 3, A and B) to continue expanding the biofilm in the lateral direction.

To reveal the underlying collective cell motion, we ensemble-averaged the velocities of cells in local proximity to one another (33). This velocity map demonstrated a distinct fountain-like flow for the WT and Rg strains (Fig. 4, B and C, and fig. S9). We observed curved mean flow streamlines near the substrate (Fig. 4, B and C, and fig. S9), which rerouted cells near the biofilm core toward the lateral expansion front.

Fountain-like flow facilitates lateral biofilm expansion along the substrate

How does fountain-like flow shape the 3D structure of a biofilm? Compared to the hypothetical case in which the radius of the biofilm increased with the average cell velocity at the substrate, the actual biofilm lateral expansion speed was more rapid (fig. S10). Thus, our calculations suggest that the fountain-like

Fig. 2. Bacterial trajectory dynamics at single-cell resolution. (**A** and **B**) Mean squared displacement (MSD) of bacterial cell trajectories versus lag time at the indicated time points for (A) WT *V. cholerae* and (B) the $\Delta vpsL$ mutant. (**C**) MSD scaling exponents ν in 90-min time windows sampled for three strains: WT, Rg, and $\Delta vpsL$. The blue arrow shows the diffusive ($\nu \approx 1$) to ballistic ($\nu \approx 2$) transition of cell trajectories at around 7 hours. (**D**) Vertical displacements versus time for cells in the WT biofilm in (C). The blue arrow marks the 7-hour time point highlighted in (C). Color indicates cell vertical velocity u_z.
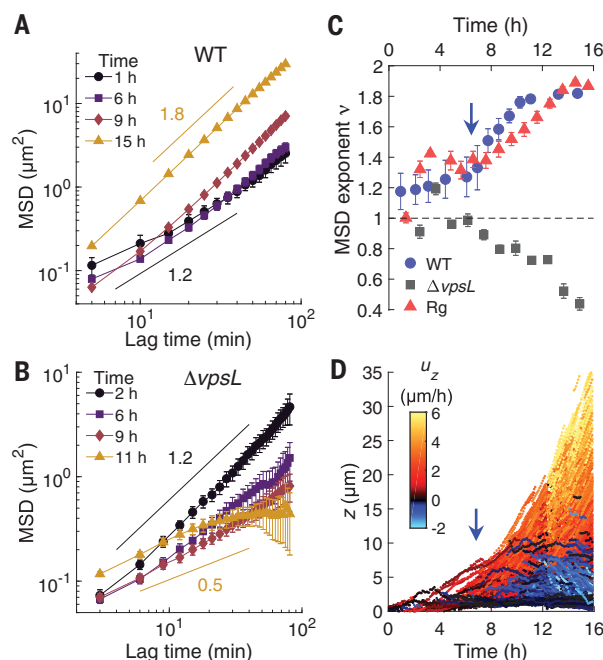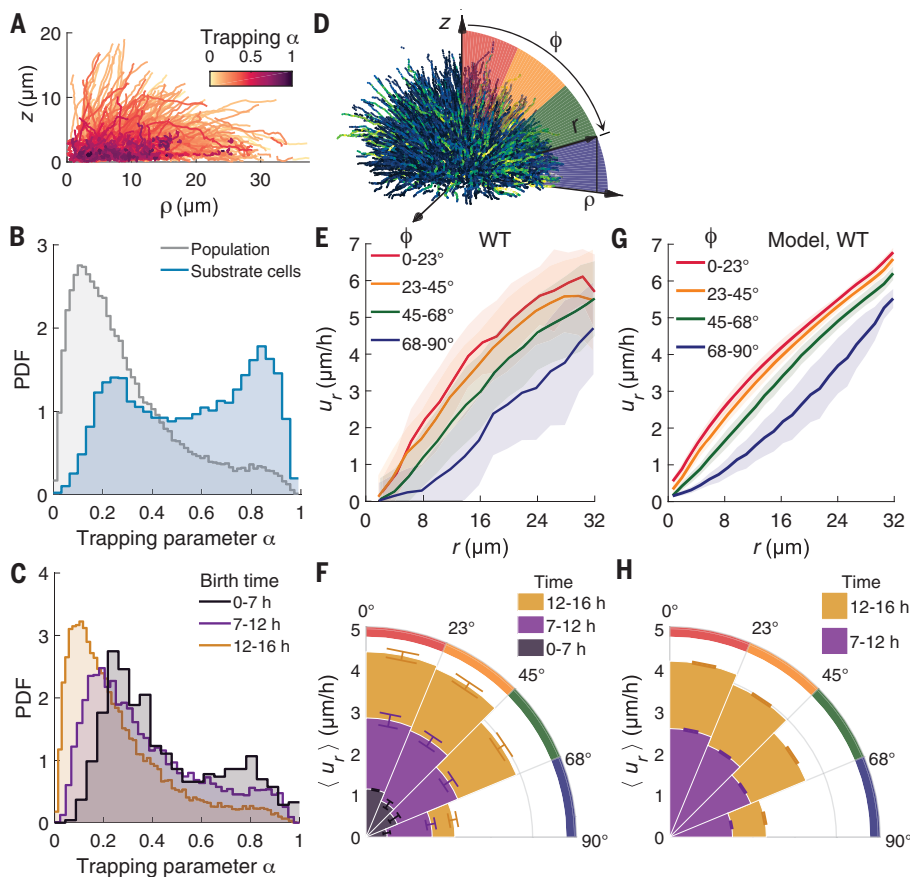
Fig. 3. Cell trapping and reduced biofilm expansion occur near the substrate. (**A**) Cell trajectories colored by trajectory trapping parameter α for all cells located within 4 μm of the substrate at any point in their trajectories. (**B**) Probability distribution function (PDF) of the trajectory trapping parameter α for WT cells near the substrate (blue) and the full population (gray). (**C**) Probability distribution function of α for different age groups at birth times of 0 to 7 hours, 7 to 12 hours, and 12 to 16 hours. In (B) and (C), n = 3 biofilm clusters. (**D**) Schematic of the spherical coordinate system. Sample trajectories are colored by mNeonGreen-μNS puncta intensity. Cells are divided into four cohorts based on their trajectory polar angle: φ = 0° to 23° (red), φ = 23° to 45° (yellow), φ = 45° to 68° (green), and φ = 68° to 90° (blue). (**E**) Radial expansion velocity u_r versus radial distance r plotted for the four φ cohorts from (D). (**F**) Polar plot of the average radial expansion velocity $\langle u_r \rangle$ of the cohorts from (D), distinguished by polar angle range in (E) during the indicated time windows. Radial sectors for each color extend from $\langle u_r \rangle = 0$ to the specified value of $\langle u_r \rangle$. Sectors are overlaid for clarity. Error bars denote standard errors. (**G**) Simulation expansion velocities corresponding to experimental results in (E). (**H**) Simulation average expansion velocities corresponding to the experimental results in (F). Error bars denote standard errors. The simulation initiates after 7 hours, that is, after the onset of the 2D to 3D transition in experiments.

flow pattern, which transported biofilm cells to the expansion front over preexisting cells that were trapped at the substrate, accelerated lateral biofilm expansion.

Collective fountain-like flows stem from growth against substrate friction

The mean flow pattern in the expanding biofilm was accurately captured by our continuum modeling. Both the model cell paths (Fig. 4D, flow path lines) and the velocity field (Fig. 4E, fig. S11, and movie S6) show clear fountain-like flow at the biofilm periphery near the substrate. Moreover, the friction parameter of the model is uniquely determined by fitting the overall biofilm shape development. A quan-

titative comparison can be made between the velocity field of the modeled biofilm and the experimental biofilm (33). The viscous fluid model captures the experimental fountain-like flow at the biofilm periphery better than the elastic solid model (fig. S11). Thus, at short times (below the cell division time scale of 30 min), cells are locally immobilized within the matrix, while at long times, the biofilm plastically deforms and flows like a liquid, akin to colloidal glasses (38, 39). The local velocity field obtained from the viscous fluid model closely agrees with the experimental cell flows (Fig. 4E, i to iii), with relative differences of ~10% (figs. S12 and S13). Thus, our minimal mechanical model of growth in the presence of substrate

friction accounts for the fountain-like flow of *V. cholerae* cells during 3D biofilm development.

Substrate friction alters biofilm morphology

Our model predicts the influence of substrate friction on overall biofilm morphology. For negligible substrate friction (Fig. 4F, top, and fig. S8), the modeled biofilm maintains a relatively flat shape and can readily spread along the substrate. For larger substrate friction (Fig. 4F, bottom, and fig. S8), however, substrate retardation of biofilm lateral expansion is pronounced, and the modeled biofilm extends farther in the vertical z direction than in the planar xy directions. The temporal evolution of the two models is compared in movie S6. This increased height-to-radius biofilm aspect ratio with increasing friction is a universal feature of growth against friction, largely independent of the specific material properties (fig. S14). Compared to WT, the Rg strain overproduces matrix components, which presumably increases friction with the substrate. This increased friction could contribute to the increased height-to-radius aspect ratio of Rg biofilms compared to that of WT (Fig. 4, B and C).

Collective cell flow and trajectory coherence require the matrix component RbmA

Although matrix components facilitate cell-cell adhesion and confer biofilm structural rigidity (16, 30, 40), their roles, if any, in modulating the mobility of individual biofilm cells and in driving overall biofilm expansion are largely unknown. To investigate their functions, we imaged yz projections of biofilm development for WT and three matrix mutants, ΔrbmA, Rg, and Rg ΔrbmA (Fig. 5, A to D). The WT and Rg cells followed coherent paths, while ΔrbmA cells moved randomly in space with uncorrelated trajectories (Fig. 5, A to C, and movies S7 and S8). To characterize the coherence of cell motion, we leveraged the concept of affine transformation (translation, rotation, shear, and dilation) and defined a nondimensional metric, the rearrangement strength χ (33), which quantifies the level of nonaffine rearrangements in the cell traces (fig. S15). For WT and Rg cells, the distribution of χ peaked at small values (Fig. 5E), with a population average close to 0.2 (Fig. 5F). By contrast, the ΔrbmA cells displayed large rearrangement strength χ values (Fig. 5E), with a population average near 0.5 (Fig. 5F), indicating highly irregular cell motions and nonaffine rearrangements during biofilm development. These cell motions were not due to swimming motility via flagellar rotation (fig. S16) but rather stemmed from growth via cell divisions and biofilm expansion. Thus, by binding cells together and to the matrix (29, 41, 42), RbmA appears to restrict the random motions of individual cells and suppresses premature separation of mother-daughter cells. These RbmA adhesive functions,
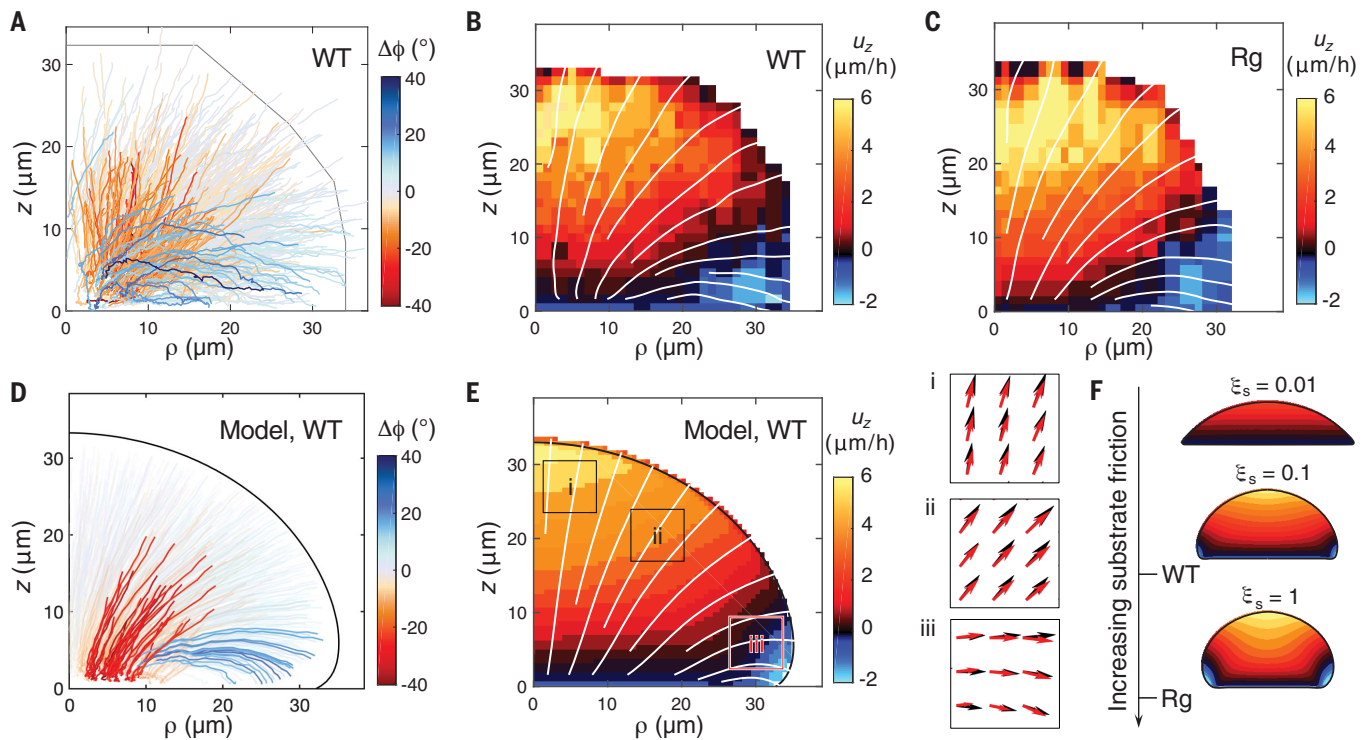
Fig. 4. Internal fountain-like cell flow patterns underlie 3D biofilm expansion.
(**A**) Cell trajectories plotted in the cylindrical coordinates with radius ρ and height z, colored by the end-to-end change in polar angle Δφ. Blue indicates cell motion reorienting toward the substrate (positive Δφ), and red indicates reorienting away from the substrate (negative Δφ). The gray curve indicates the biofilm boundary. (**B** and **C**) Heatmaps of locally averaged vertical cell velocity u_z with streamlines (white) for the internal flow of cells for (B) WT *V. cholerae* and (C) the Rg biofilms with approximately 1500 puncta. (**D**) Modeled cell trajectories in a viscous biofilm plotted in cylindrical coordinates. Color code as in (A). (**E**) Heatmap of vertical velocity u_z with flow streamlines (white) of the modeled biofilm. The dimensionless surface friction parameter $\xi_s = 0.5$ was chosen by fitting the overall shape of the modeled biofilm to that of the experimental biofilm. Insets i, ii, and iii show local velocity vectors of the modeled biofilm [black arrows, data from (E)] compared with those of the WT experimental biofilm [red arrows, data from (B)]. (**F**) Morphologies of modeled biofilms at the indicated substrate frictions ξ_s. WT corresponds to $\xi_s = 0.5$ and Rg corresponds to $\xi_s = 3.2$. Colors indicate local vertical velocity u_z. Color code as in (E).

however, do not constrain the overall outward movement of cells, and thus the overall expansion of the biofilm. The collective fountain-like flow thus enabled biofilm expansion while maintaining cell trajectory coherence.

Cell motion coherence in the rbmA *mutant can be partially rescued through elevated expression of other matrix genes*

Introduction of the mutation that confers the Rg biofilm phenotype to *V. cholerae* elevated expression of genes encoding matrix components compared to the WT (Fig. 5G). In turn, global morphological changes occurred (Fig. 4, B and C) along with a reduced cell density at the biofilm core (fig. S7, D and H) and increased substrate friction (Fig. 4F and fig. S8). We wondered how increased matrix production influences the cell trajectories in biofilms. Introduction of the Rg mutation into the Δ*rbmA* strain drastically elevated expression of *rbmC*, *bap1*, and *vpsL*, encoding the other matrix components (Fig. 5G). Moreover, cell trajectory coherence was increased, and rearrangement strength was decreased (Fig. 5, D and E). Specifically, the rearrangement

strength of cells possessing the Rg and Δ*rbmA* mutations was intermediate between that of the Δ*rbmA* single mutant and the WT (Fig. 5, E and F). Thus, some or all of the matrix components encoded by *rbmC*, *bap1*, and *vpsL* must act synergistically with RbmA to mediate the coherence of individual cell trajectories and drive collective flow in biofilms.

Outlook

In this study, we tracked cell lineages and trajectories in space and time throughout bacterial biofilm development to provide insight into how these ancient multicellular structures form from a single founder cell. By combining dual-view light-sheet microscopy, intracellular fluorescent puncta labeling, mutagenesis, quantitative reverse transcription polymerase chain reaction (qRT-PCR), and mathematical modeling, we established mechanistic principles underpinning cell position fates and collective cell motions during biofilm formation (fig. S17). Spatiotemporal imaging with high resolution allowed us to uncover two distinct cell behaviors in biofilms: substrate trapping and ballistic outward expansion, which together

determine each cell's final position in the mature biofilm. We suspect that a cell's ultimate position will determine its local environment and gene expression pattern and, thus, whether it remains or exits the community during subsequent biofilm dispersal. Furthermore, we identified an emergent collective fountain-like cellular flow that drives biofilm expansion. This group-transport pattern enables cells at the biofilm core to leapfrog cells trapped at the substrate, allowing biofilm expansion in the face of substrate friction. We linked the roles of extracellular matrix and mechanical forces to individual cell trajectories and dynamics during biofilm expansion. Specifically, RbmA maintains the coherence of collective cellular flow, which allows the biofilm to expand on surfaces while maintaining its structural robustness.

It remains to be investigated whether biofilm cells are capable of modulating the production of the Bap1 and RbmC matrix components responsible for biofilm-substrate interactions to produce distinct cellular flow patterns and, in turn, biofilm architectures that exhibit superior function in particular environments.
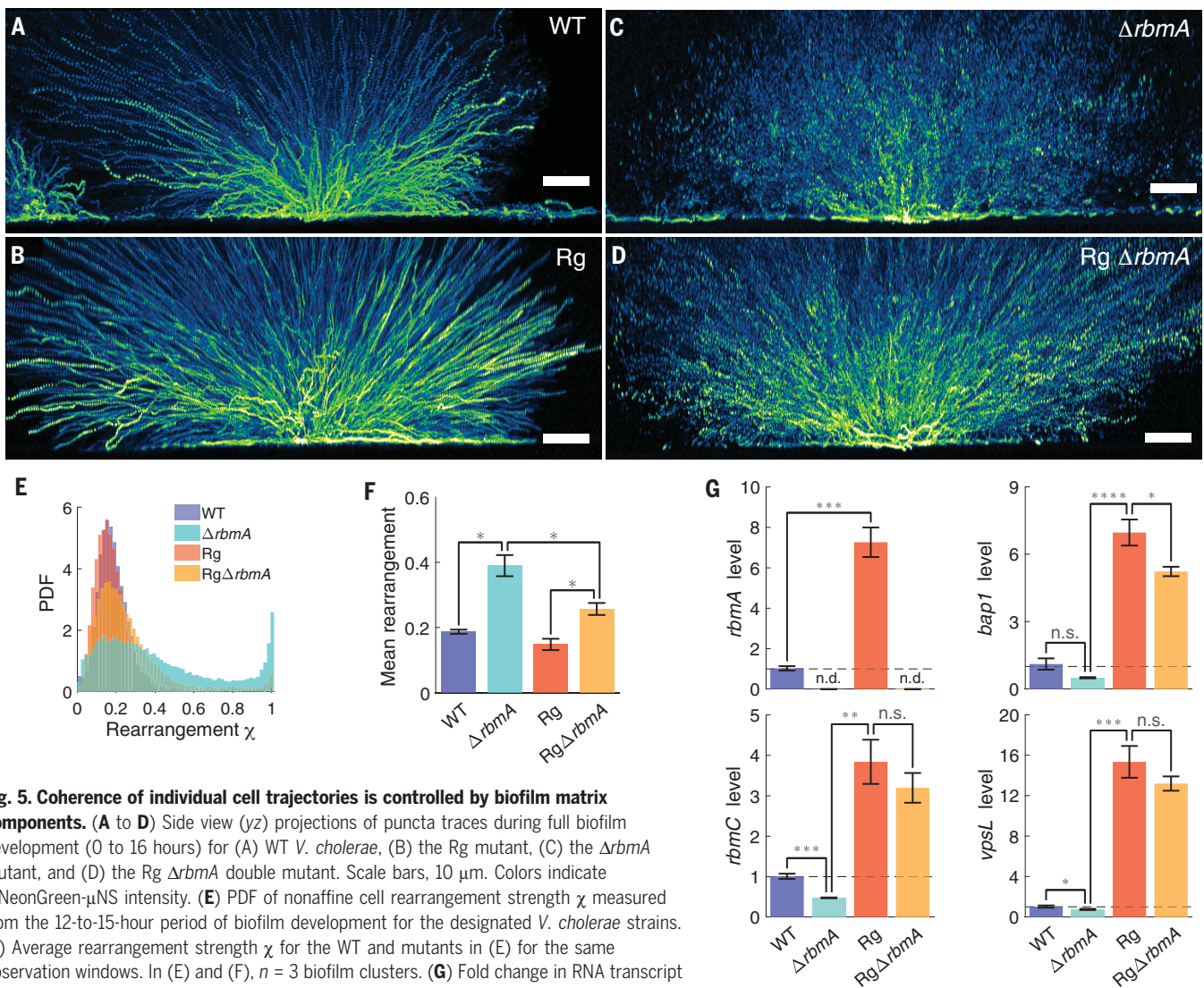
Fig. 5. Coherence of individual cell trajectories is controlled by biofilm matrix components. (**A** to **D**) Side view (yz) projections of puncta traces during full biofilm development (0 to 16 hours) for (A) WT *V. cholerae*, (B) the Rg mutant, (C) the ΔrbmA mutant, and (D) the Rg ΔrbmA double mutant. Scale bars, 10 μm. Colors indicate mNeonGreen-μNS intensity. (**E**) PDF of nonaffine cell rearrangement strength χ measured from the 12-to-15-hour period of biofilm development for the designated *V. cholerae* strains. (**F**) Average rearrangement strength χ for the WT and mutants in (E) for the same observation windows. In (E) and (F), n = 3 biofilm clusters. (**G**) Fold change in RNA transcript levels for *rbmA*, *bap1*, *rbmC*, and *vpsL* relative to that in the WT in the designated strains measured by qRT-PCR (n = 3 biological and 2 technical replicates). DNA gyrase (*gyrA*) and the WT strain transcript levels were used for normalization. Colors as in (E). Dashed lines represent the WT level. Unpaired *t*-tests with Welch's correction were performed for statistical analyses. In (F) and (G), *P* values are denoted as *$P < 0.05$; **$P < 0.01$; ***$P < 0.001$; ****$P < 0.0001$; n.s., $P > 0.05$; and n.d., not detected.

Our modeling demonstrates that the magnitude of substrate friction forces, which depend on biofilm matrix components, can influence the overall biofilm morphology, in particular the height-to-radius aspect ratio. These collective cellular flow patterns and cell-matrix–substrate interaction principles may be relevant in other prokaryotic and eukaryotic systems and could underpin multicellular development and organization.

REFERENCES AND NOTES

1. M. J. F. Barresi, S. F. Gilbert, *Developmental Biology* (Oxford Univ. Press, ed. 12, 2019).
2. G. O'Toole, H. B. Kaplan, R. Kolter, *Annu. Rev. Microbiol.* **54**, 49–79 (2000).
3. L. Hall-Stoodley, J. W. Costerton, P. Stoodley, *Nat. Rev. Microbiol.* **2**, 95–108 (2004).
4. P. J. Keller, A. D. Schmidt, J. Wittbrodt, E. H. K. Stelzer, *Science* **322**, 1065–1069 (2008).
5. K. McDole *et al.*, *Cell* **175**, 859–876.e33 (2018).
6. K. Drescher *et al.*, *Proc. Natl. Acad. Sci. U.S.A.* **113**, E2066–E2072 (2016).
7. J. Yan, A. G. Sharo, H. A. Stone, N. S. Wingreen, B. L. Bassler, *Proc. Natl. Acad. Sci. U.S.A.* **113**, E5337–E5343 (2016).
8. D. Ben-Zvi, B. Shilo, A. Fainsod, N. Barkai, *Nature* **453**, 1205–1211 (2008).
9. B. Monier *et al.*, *Nature* **518**, 245–248 (2015).
10. V. E. Deneke *et al.*, *Cell* **177**, 925–941.e17 (2019).
11. P. S. Stewart, M. J. Franklin, *Nat. Rev. Microbiol.* **6**, 199–210 (2008).
12. E. Karatan, P. Watnick, *Microbiol. Mol. Biol. Rev.* **73**, 310–347 (2009).
13. S. Mukherjee, B. L. Bassler, *Nat. Rev. Microbiol.* **17**, 371–382 (2019).
14. A. Persat *et al.*, *Cell* **161**, 988–997 (2015).
15. Y. Wan, K. McDole, P. J. Keller, *Annu. Rev. Cell Dev. Biol.* **35**, 655–681 (2019).
16. J. K. Teschler *et al.*, *Nat. Rev. Microbiol.* **13**, 255–268 (2015).
17. C. D. Nadell, K. Drescher, K. R. Foster, *Nat. Rev. Microbiol.* **14**, 589–600 (2016).
18. H. C. Flemming *et al.*, *Nat. Rev. Microbiol.* **14**, 563–575 (2016).
19. J. Pawley, Ed., *Handbook of Biological Confocal Microscopy* (Springer, ed. 3, 2006).
20. Y. Wu *et al.*, *Nat. Biotechnol.* **31**, 1032–1038 (2013).
21. A. Kumar *et al.*, *Nat. Protoc.* **9**, 2555–2573 (2014).
22. B. C. Chen *et al.*, *Science* **346**, 1257998 (2014).
23. T. L. Liu *et al.*, *Science* **360**, eaaq1392 (2018).
24. T. J. Broering *et al.*, *J. Virol.* **79**, 6194–6206 (2005).
25. B. R. Parry *et al.*, *Cell* **156**, 183–194 (2014).
26. A. Seminara *et al.*, *Proc. Natl. Acad. Sci. U.S.A.* **109**, 1116–1121 (2012).
27. F. H. Yildiz, G. K. Schoolnik, *Proc. Natl. Acad. Sci. U.S.A.* **96**, 4028–4033 (1999).
28. J. C. N. Fong, K. A. Syed, K. E. Klose, F. H. Yildiz, *Microbiology* **156**, 2757–2769 (2010).
29. C. Absalon, K. Van Dellen, P. I. Watnick, *PLOS Pathog.* **7**, e1002210 (2011).
30. V. Berk *et al.*, *Science* **337**, 236–239 (2012).
31. D. R. Smith *et al.*, *Proc. Natl. Acad. Sci. U.S.A.* **112**, 10491–10496 (2015).
32. B. Lim, S. Beyhan, J. Meir, F. H. Yildiz, *Mol. Microbiol.* **60**, 331–348 (2006).
33. Materials and methods are available as supplementary materials.
34. I. Klapper, C. J. Rupp, R. Cargo, B. Purvedorj, P. Stoodley, *Biotechnol. Bioeng.* **80**, 289–296 (2002).
35. J. Yan *et al.*, *Adv. Mater.* **30**, e1804153 (2018).

36. S. G. V. Charlton *et al.*, *J. Bacteriol.* **201**, e00101-19 (2019).
37. C. Fei *et al.*, *Proc. Natl. Acad. Sci. U.S.A.* **117**, 7622–7632 (2020).
38. P. Schall, D. A. Weitz, F. Spaepen, *Science* **318**, 1895–1899 (2007).
39. G. L. Hunter, E. R. Weeks, *Rep. Prog. Phys.* **75**, 066501 (2012).
40. H. C. Flemming, J. Wingender, *Nat. Rev. Microbiol.* **8**, 623–633 (2010).
41. J. C. N. Fong *et al.*, *eLife* **6**, e26163 (2017).
42. J. C. N. Fong, K. Karplus, G. K. Schoolnik, F. H. Yildiz, *J. Bacteriol.* **188**, 1049–1059 (2006).
43. B. Qin *et al.*, Code and dataset for: Cell position fates and collective fountain flow in bacterial biofilms revealed by light-sheet microscopy, Zenodo (2020); https://doi.org/10.5281/zenodo.3828028.

SUPPLEMENTARY MATERIALS

science.sciencemag.org/content/369/6499/71/suppl/DC1
Materials and Methods
Supplementary Text
Figs. S1 to S17
Tables S1 to S3
References (*44–77*)
MDAR Reproducibility Checklist
Movies S1 to S8

View/request a protocol for this paper from *Bio-protocol*.

Science

Cell position fates and collective fountain flow in bacterial biofilms revealed by light-sheet microscopy

Boyang Qin, Chenyi Fei, Andrew A. Bridges, Ameya A. Mashruwala, Howard A. Stone, Ned S. Wingreen and Bonnie L. Bassler

Biofilm formation from cell fountains

Bacteria form three-dimensional communities called biofilms that are ubiquitous in nature and underlie human infections. Medically, biofilms are problematic because they protect resident cells from antibiotics. Although biofilms have been intensively studied, we do not understand how they develop cell by cell. Micron-sized bacteria are densely packed within biofilms, making it exceptionally challenging to track their movements. Qin *et al.* studied biofilm formation in the pathogen and model biofilm former *Vibrio cholerae* (see the Perspective by Dal Co and Brenner). The authors combined light-sheet microscopy with cell labeling to map the trajectories of a biofilm founder cell and its descendants in space and time as they built a biofilm. The findings revealed that as the bacteria reproduce, a bacterial "fountain" drives biofilm expansion and dictates the final positions of the offspring.
Science, this issue p. 71; see also p. 30

ARTICLE TOOLS	http://science.sciencemag.org/content/369/6499/71
SUPPLEMENTARY MATERIALS	http://science.sciencemag.org/content/suppl/2020/06/10/science.abb8501.DC1
RELATED CONTENT	http://science.sciencemag.org/content/sci/369/6499/30.full
REFERENCES	This article cites 72 articles, 18 of which you can access for free http://science.sciencemag.org/content/369/6499/71#BIBL
PERMISSIONS	http://www.sciencemag.org/help/reprints-and-permissions